

1 **Deep crustal architecture of the Parnaíba basin of**
2 **NE Brazil from receiver function analysis:**
3 **Implications for basin subsidence.**

5 **Diogo Loc^{1*}, Verónica Rodríguez-Tribaldos², Jordi Julià¹ & Nicholas White²**

6

7 *¹Departamento de Geofísica, Universidade Federal do Rio Grande do Norte, Capim
8 Macio, Natal, CEP 59078-970, Brazil*

9 *²Bullard Laboratories, Department of Earth Sciences, University of Cambridge, Madingley
10 Rise House, Madingley Road, Cambridge, CB3 0EZ, UK*

11 **Corresponding author (e-mail: locdiogo@gmail.com)*

12

13 **Abstract**

14 We investigate the crustal architecture of the Parnaíba basin of NE Brazil by analyzing
15 receiver functions along a ~500 km-long transect. The transect consisted of 9 broad-
16 band seismographic stations interspaced at about 70 km distance. The stations were de-
17 ployed under the Parnaíba Basin Analysis Project (PBAP), a multi-disciplinary, multi-
18 institutional effort funded by BP Energy do Brasil. Our results reveal that crustal thickness
19 is quite uniform along the transect, around 40 - 43 km thick, with crustal S-velocities
20 well under 4.2 km/s throughout the entire crustal column. Bulk Vp/Vs ratios vary be-
21 tween 1.69 and 1.75, with sporadic occurrences of ratios slightly above 1.80. The uni-
22 formity of the basement's crust under the basin is consistent with minimal stretching of
23 the lithosphere during the development and further evolution of this basin, as already
24 suggested by seismic profiling and surface geology. Moreover, relatively small Vp/Vs ra-
25 tios and slow S-velocities suggest a felsic-to-intermediate composition for the crust, and
26 rule out the presence of a massive mafic load in the lower crust driving subsidence of the
27 basin. Deeper loads in the lithospheric mantle and/or convecting processes in the under-
28 lying asthenosphere might be at play to explain the origin and evolution of this basin.

29

30

31 **Keywords:** Cratonic basin, South America, Crustal architecture

32

33

34 **Supplementary material:** [description of material] is available at <https://doi.org/xxxx>.
35 [GSL will assign the doi and url unless you already have one]

36

37

38 The genesis and evolution of large basins in the stable interiors of continents is an impor-
39 tant geological process that is not easily understood within the Plate Tectonics paradigm.
40 The basin-forming mechanism and tectonic history of these basins has long been debated,

and no clear consensus has yet emerged as demonstrated by the varied range of mechanisms that aim at explaining their intriguing origin. Kaminski and Jaupart (2000) showed that the four major intracratonic basins of North America, the Hudson Bay, Michigan, Illinois and Williston basins, have similar ages and are close to one another, however, they exhibit different subsidence histories characterised by different time-scales and sediment thicknesses. Cloetingh and Burov (2011) cite that an important feature in the depositional history of cratonic basins is the prolonged intervals of low rate subsidence alternating with fast subsidence rates, often related with orogenic activity at plate boundaries. There are a large variety of mechanisms to explain cratonic basins, Hartley and Allen (1994) divided these hypothesis in five classes: lithospheric stretching and subsequent thermal contraction; crustal and mantle phase changes, metamorphism and intrusion; changes of in-plane stress and tectonic rejuvenation; convective instabilities in the mantle; and, subaerial erosion of uplifts.

The Parnaíba basin is one of three large Paleozoic basins in stable South America, together with the Paraná basin of SE Brazil and the Amazon basin in the northern portion of the continent. The basin is commonly described as a large, sag-type cratonic basin, with a roughly circular shape and a depocenter in the center of the basin reaching up to 3.5 km depth (Góes and Feijó, 1994; Vaz et al., 2007; Daly et al., 2014). It is agreed that initial subsidence of the basin occurred in an intra-continental setting during Paleozoic times, with the proto-basin being framed by three large cratonic masses (Figure 1): Amazon to the West, São Luiz-West Africa to the North, and Sāo Francisco-Congo to the South and East (Almeida et al., 1981; Brito Neves et al., 1984; Cordani et al., 2009; Brito Neves and Fuck, 2013; Cordani et al., 2013); however, the physical mechanism of subsidence is a matter of debate. There are two main mechanisms proposed to explain the subsidence history of the basin: a thermal evolution based on deeper unconformities at the base of the basin combined with magmatic episodes, (Daly et al., 2014), and, a mechanical-thermal mechanism based on residual gravity, residual magnetic, and pseudo-gravity data that indicate the presence of a complex systems of Eopaleozoic rifts. Detailed knowledge of its deep crustal architecture is therefore critical to discriminate among these competing models.

Very little is known about the deep, crustal architecture of this enigmatic cratonic basin, most of our current knowledge being restricted to low-resolution, continental-scale studies (Feng et al., 2004, 2007; Lloyd et al., 2010; van der Meijde et al., 2013; Assumpção et al., 2013b,a; Uieda and Barbosa, 2017), and a single seismic reflection profile crossing the basin in the EW direction (Daly et al., 2014). The continental-scale studies estimated a thinnest crust under Proterozoic Provinces (30–35 km), while the thickest crust is found beneath the cratons, e.g. Amazon and São Francisco, (41 ± 4 km), and cratonic basins, e.g. Paraná and Parnaíba, (42 ± 4 km). (Daly et al., 2014) showed three crustal blocks defined by distinct seismic facies and geometry. The three crustal blocks are underlain by a variably imaged Moho, ≈ 40 km in the western side and in the eastern part is ≈ 35 km. In the central Parnaíba block the Moho relief is indistinguishable, being imaged only in eastern side of the block.

In this work, we characterize the deep, crustal architecture of the Parnaíba basin by mapping subsurface seismic discontinuities with teleseismic P-wave receiver functions (Langston, 1979) at 9 broadband stations in the basin (Figure 1). We present estimates of crustal thickness and V_p/V_s ratio at each station obtained through the $H\kappa$ -stacking procedure of (Zhu and Kanamori, 2000), along with S-wave velocity-depth profiles obtained from the joint inversion of receiver functions and surface-wave dispersion velocities (Julià et al., 2000, 2003),

and a depth-migrated cross-section using the Common Conversion Point (CCP) stacking of (Frassetto et al., 2010). The $H\kappa$ -stacking analysis reveals that the crust is 40-42 km thick and that bulk V_p/V_s ratios are in the 1.69-1.75 range (although they may locally reach values of 1.81-1.82). The CCP stacking migrated cross-section displays a relatively flat Moho at \approx 40 km depth, consistent with the $H\kappa$ -stacking values. The velocity-depth profiles show a simple crust, consisting of a 2-3 km thick sedimentary package overlying a 3.5-3.6 km/s crust down to 25-30 km depth, where S-velocities gradually increase to \approx 4.0 km/s near Moho depths. The crust-mantle boundary is gradational under most of the stations, and uppermost mantle velocities are around 4.5 km/s. Our findings are consistent with minimal mechanical stretching of the basin's underlying crust and thermal cooling as the driving mechanism for subsidence (Daly et al., 2014). They are inconsistent with models invoking a vertical load in the lower crust [*Watts et al.*, this volume], although a vertical load in the lithospheric mantle cannot be ruled out. Dynamic subsidence related to deep convecting processes in the asthenosphere could also be playing a role.

101

102

103 Geology and Tectonic Setting

104 The depositional history of the Parnaíba basin is built on five primary tectono-sedimentary
 105 sequences and two magmatic pulses separated by regional unconformities (Góes and Feijó,
 106 1994; Vaz et al., 2007). The geologic history starting in the Early Paleozoic finalizing with the
 107 Cretaceous sequence (see Figure 1). The basin is filled out of thick epicontinental sequences,
 108 primarily siliciclastic. The depositional history starts in Cambrian–Ordovician period with
 109 a thick siliciclastics and volcanoclastic rocks. The Silurian period is characterized by the
 110 deposition of alternate thin and thick siliciclastics from continental environment to shallow
 111 marine. The Meso Devonian/Carboniferous deposits arising from a transition of continental
 112 syneclyse to shallow marine ambient. The Neocarboniferous/Permotriassic sediments also
 113 is derived from continental syneclyse to shallow marine ambient, showing a desertification
 114 process in the end of the period. Juro-Cretaceous sequence presents sediments deposited
 115 during the beginning of Pangea break-up. Consequently, two expressive magmatic events,
 116 Mosquito and Sardinha formation, are observed interfingering the sedimentary column. Ma-
 117 jor volcanic exposures occur along E–W direction in the central part of the basin, and
 118 secondary exposures occur on its northeast corner and southeast edge, as shown in Figure 1.
 119 Furthermore, Cenozoic alluvial and aeolian deposits cover large areas of the Parnaíba basin.

120 Cordani et al. (2013); Daly et al. (2014); de Castro et al. (2014) presented the basin
 121 encircled by sutures zones associated with cratonic blocks collisions, as shown in the Figure
 122 1. On the eastern side of the basin, the Araguaia suture zone represents the final Neo-
 123 proterozoic collision between the Amazonian craton and the pre-Neoproterozoic Parnaíba
 124 block (Fuck et al., 2008; Brito Neves and Fuck, 2014). On the eastern side of the basin, the
 125 Transbrasiliano Lineament, a continental-scale discontinuity characterized by strong mag-
 126 netic anomalies and by low S wave velocities in the mantle controls the internal rift geometry
 127 and form a 150 km wide rift zone (Fairhead and Maus, 2003; Feng et al., 2004; Brito Neves
 128 and Fuck, 2014). On the septentrional boundary, the Gurupi Belt represents the defor-
 129 mation zone between the Parnaíba block and São Luís craton. This belt is a sequence of
 130 Paleoproterozoic rock assemblages reworked in the Neoproterozoic during a Brasiliano phase
 131 (Klein et al., 2005). These lineaments also form Precambrian lithospheric-scale boundaries

132 that were identified in a deep crustal seismic reflection profile across the Parnaíba basin
 133 and represent the collisional sutures of the Amazonian and the São Francisco cratons (Daly
 134 et al., 2014; de Castro et al., 2014).

135 The Parnaíba basin is a cratonic basin located on rigid lithosphere, tectonically stabilized
 136 in the latest Precambrian/early Palaeozoic, and its subsidence was first attributed to thermal
 137 cooling of a central cratonic block now hidden under the basin's sedimentary sequences
 138 (Brito Neves et al., 1984). Thermal cooling of a central cratonic block - although of different
 139 geometry - was also proposed by Daly et al. (2014). According this authors the Parnaíba
 140 basin overlies a marked, regional, subplanar unconformity that crosses three crustal blocks
 141 (Araguaia, Parnaíba and Borborema) and suggests a scale of basin larger than that which is
 142 preserved today. Cordani et al. (2009); de Castro et al. (2016) call attention to shear zones
 143 as probable main protagonist in the evolution of the Parnaíba basin. Daly et al. (2014) state
 144 that the profound unconformity at the base of the Phanerozoic section and the two major
 145 igneous episodes in Early Jurassic and Early Cretaceous are important components of the
 146 basin evolution, thermal history, and tectonic context.

147 Alternatively, a number of models have advocated an initial stage of mechanical stretching
 148 of the basin's underlying lithosphere to explain subsidence (Fuck et al., 2008; Cordani
 149 et al., 2009; de Castro et al., 2014). These authors based in geophysical data state that
 150 the basement beneath the Parnaíba basin was subdivided into a couple of crustal blocks
 151 in accordance with their magnetic and gravity signatures. As said by Brito Neves et al.
 152 (1984); Fuck et al. (2008); Cordani et al. (2009); de Castro et al. (2014) beneath the Par-
 153 naíba basin there are some crustal massifs that represents an old continental fragment over
 154 a relatively thickened crust, around 42 km, in relation to surrounding crustal zones and its
 155 existence has been proposed on the basis of geophysical evidence in addition to petrogra-
 156 phy and geochronology of the basement rocks. Cordani et al. (2009) said that in border
 157 of the basin these blocks has been dated with radiometric ages close to Paleoproterozoic
 158 era, but the block beneath the basin remains uncharted. de Castro et al. (2014) con-
 159 cluded that rifting was the driving mechanism for the subsidence of the Phanerozoic basin.

160

161

162 Data and data processing

163 The dataset utilized in this work was acquired by the Universidade Federal do Rio
 164 Grande do Norte and the University of Cambridge as part of the broader Parnaíba Basin
 165 Analysis Project (PBAP), a multi-disciplinary effort funded by BP Energy do Brasil that
 166 aims at improving our current knowledge of the origin and evolution of this large cratonic
 167 basin. Our dataset is composed by 8 stations equipped with Nanometrics three-component
 168 Meridian Compact Posthole sensors, with a frequency band between 120 seconds to 108 Hz
 169 and one station using three-component **GURALP - PEGAR COM A**
170 VERONICA sensor, all stations works with sampling at 100 samples per second
 171 (s.p.s.). These seismic stations are localized in the Northeast of Brazil forming a transect
 172 with 600 km width and a interstation spacing of 50 to 70 km, as seen in Figure 1. The
 173 majority of these stations has been operating since March 2016. They will keep recording
 174 until the end of this project late 2018. In the Table 1 is presented the location and the
 175 recording time of each station.

In order to develop receiver function estimates for each of the seismic stations in the broadband deployment, seismic sources with epicentral distances ranging between 30° and 90° and magnitudes above 5.5 mb were considered. The coda immediately trailing teleseismic P-wave arrivals is the combination of the earthquake's source time history and near-source propagation, the instrument response, and propagation near the receiver (Langston, 1979; Ammon, 1991). Receiver functions are obtained by deconvolving the vertical component of the teleseismic P-coda from the corresponding radial component, effectively removing the signature of the source and instrument response from the deconvolved time-series. What remains are secondary P-to-S converted waves at seismic discontinuities underlying the receiver, so analysis of their amplitudes and travel-times can be utilized to develop constraints on the seismic structure under the station (Owens et al., 1984; Ammon et al., 1990). Moreover, the deconvolution process equalizes the teleseismic waveforms and they can be stacked to produce robust estimates of the receiver response under a seismic station. The deconvolution procedure can also be applied to the transverse component of the teleseismic P-coda. The transverse component should be identically zero for isotropic, laterally homogenous propagating media, so the observation of P-to-S conversion in the transverse receiver function can be used as diagnostic for dipping or anisotropic structures under the station (Cassidy, 1992).

To effectively compute receiver function estimates, the selected seismograms were cut 10 s before and 120 s after the P-wave arrival, demeaned, detrended, tapered with a 5% cosine window and filtered between 0.05 Hz to 5 Hz, to remove low-frequency noise and to avoid aliasing. After this, the waveforms were re-sampled to 10 Hz to facilitate the processing. According to the great-circle path, the horizontal components were rotated at each seismogram generating the radial and transverse components. To obtain the receiver functions the radial and transversal components were deconvolved from the vertical component, following the principles of Langston (1979). The deconvolution removes the signature of the common source time function and instrument response from the resulting trace, leaving only the signature of the near-receiver structure. The iterative deconvolution procedure of Ligorría and Ammon (1999) was used, with 500 iterations and a Gaussian filter width of 2.5, to obtain a frequency band that allow identify the crustal P-to-S conversions and reverberations. The quality control of the receiver functions was made by computing the percent root-mean-square (RMS) between the observed radial component and the predicted radial component, implemented in the Ligorría and Ammon (1999) procedure, and a visual inspection to avoid incongruous values of amplitude. RMS values recoveries of the observed radial component under 90% were rejected as well as anomalous amplitudes in the receiver functions, in both radial and transverse receiver functions. From 744 waveforms we selected 119 for further analysis after the cross-check, as seen in Figure 2.

Examples of stacked radial and transverse receiver functions in the Parnaíba basin are displayed in Figure 2, right and left panels show radial and transversal receiver functions, respectively, for each station. The number of waveforms stacked for each station are presented in round brackets and the maximum and minimum amplitude values of the receiver functions utilised are plotted in shaded gray. A simple inspection of the waveforms reveals important properties of the propagating medium beneath each station. We observe that stacked radial receiver functions decay rapidly in amplitude, indicating the loss of energy through the time, that showing a good behavior of the radial receiver function. Oftentimes this behavior is related with a relatively homogeneous crust. The transverse components are generally small and have nearly constant amplitude comparing with the

223 radial component, indicating that lateral variations in the structure are small, for a laterally
 224 homogeneous media is expected a transverse receiver function have an amplitude equal
 225 to zero. Figure 2 displays small transverse amplitudes indicating that the medium under
 226 the PBAP stations can be approximate as laterally homogeneous and isotropic, except the
 227 BDCO station that presents high unrepresentative amplitude values in both components.
 228 The radial receiver functions are characterized by a large peak at zero lag time, corre-
 229 sponding to the direct P-wave, followed by a number of peaks and troughs associated to
 230 secondary P-to-S conversions. Comparing the PBAP stations radial amplitudes in the 2,
 231 we see apparent peaks and troughs between 1 and 3 s caused by the P-wavefront imping-
 232 ing on a sedimentary structure. Finally, the P wave converted in S phase generated at
 233 the Moho is generally apparent in all the waveforms at about 5 s, but the reverberated
 234 phases in the bulk crustal structure are generally harder to identify in some stations. The
 235 wavelengths of the reverberated phases are shorter than those of the Ps phase, and a gradua-
 236 tional crust–mantle boundary could reduce their amplitudes significantly (Julià et al., 2000).

237

238

239 Crustal Architecture

240 Receiver functions can be inverted for retrieve the crustal S wave velocity profile beneath
 241 the station, but the inversion process is nonlinear and the solution is nonunique (Ammon
 242 et al., 1990). To obtain a reliable velocity structure, we need to include additional informa-
 243 tion about the velocities of the crust, as dispersion curves of surface waves or information
 244 about the average P-wave velocity for continental areas. In this paper, we present crustal
 245 thickness, bulk Vp/Vs ratio and variation of S-velocity with depth based on observed receiver
 246 functions developed for the 9 broadband stations in the Parnaíba basin with three separate
 247 techniques. Ultimately, we cross-checked the generated results to validate the model for the
 248 crustal
 249 architecture.

250

250 H- κ stacking

251 Crustal thickness and Vp/Vs ratio can be estimated from receiver functions utilizing the
 252 H- κ stacking approach of Zhu and Kanamori (2000). This procedure performs a grid-search
 253 over a stacking surface that is built by summing a weighted combination of Ps, PpPs and
 254 PpSs+PsPs amplitudes from individual receiver function estimates. Zhu and Kanamori
 255 (2000) explains that three P-to-S converted phases are: Ps, a P-to-S conversion upon re-
 256 fraction at the base of the layer; PpPs (1st multiple), reverberation with P-to-S conversion
 257 upon reflection at the base of the layer; and PsPs+PpSs (2nd multiple), reverberations with
 258 two P-to-S conversions. The summation is performed along phase-moveout curves for the
 259 three P-to-S conversions, which are computed after assuming a simple layer-over-half space
 260 model for the receiving structure. During the calculation, the P-velocity for the layer has
 261 to be specified *a priori*, while thickness and Vp/Vs ratio are left as free parameters. The
 262 summation of amplitudes is then performed according to

263

$$s(H, \kappa) = w_1 \times r(t_1) + w_2 \times r(t_2) - w_3 \times r(t_3) \quad (1)$$

where $r(t)$ is the radial receiver function, $t1$, $t2$ and $t3$ are the predicted Ps, PpPs, and PsPs+PpSs arrival times corresponding to crustal thickness H and Vp/Vs ratio κ . The w_i are weighting factors, and $\sum w_i = 1$. Zhu and Kanamori (2000) show that the $s(H, \kappa)$ reaches a maximum when all three phases are stacked coherently with the correct H and κ , as seen in the a) and b) in Figure 3. Crustal thickness and Vp/Vs ratios are varied within prescribed ranges and the maximum in the $H\text{-}\kappa$ stacking surface is taken as an estimation of crustal thickness and bulk Vp/Vs ratio under the station.

We assigned values of 0.4, 0.3, and 0.3, to all three phases, respectively, when all phases are surely observed. Moreover, when some phase are questionable we assigned values of 0.2 to this phase. Increase the weight of the first phase is coherent with the results of the Figure 2, because the first phase is clearly perceptible in all seismograms. The another reverberations are not evident in some seismograms and we need to handle with this trade-off to build a trustworthy estimate. The methodology of Zhu and Kanamori (2000) requires the assumption of a P-wave velocity, which is uncharted to the basin until now. To avoid this incertitude, we took values between 6.3 to 6.6 km/s to observe the variation of the estimates, as can be observed in the Table 2. Confidence bounds (2σ) for crustal thickness and bulk Vp/Vs ratio were developed after bootstrapping the receiver function dataset with 200 replications (Efron and Tibshirani, 1991).

Examples of the $H\text{-}\kappa$ stacking procedure at select stations in Parnaíba basin, two broadband stations in oposite sides on the transect, are given in Figure 3. The a,c panels display the $H\text{-}\kappa$ stacking surface and b,c panels display the receiver functions sorted by backazimuth, with the Ps, PpPs, and PsPs+PpSs arrival times. Zhu and Kanamori (2000) state that a clear Ps conversion and at least one apparent multiple guarantee well-constrained estimates for crustal thickness and Vp/Vs ratio. Note that the b panel shows each P-to-S phase for the STSR station, then the estimates for crustal thickness and to Vp/Vs ratio are well-constrained, 38.6 ± 0.2 km and 1.69 ± 0.01 , respectively. On the other hand, at GRJU station is harder to identify the first and second multiples (panel d), the estimated crustal thickness and Vp/Vs ratio was 40.9 ± 1.4 km and 1.83 ± 0.05 , respectively. This measure is valid, but it is not precise like the STSR station.

A summary of crustal thicknesses and bulk Vp/Vs ratios for the PBAP sampling the Parnaíba basin is given in Table 2. The crustal thicknesses range between 38 and 44 km and are generally constrained within 3 km. Overall, these values are in excellent agreement with the estimates from previous continental scale studies (Feng et al., 2007; Lloyd et al., 2010; Assumpção et al., 2013a; Uieda and Barbosa, 2017). The Vp/Vs ratio are more variable and less constrained, many measures range between 1.69 and 1.76 and have confidence bounds below ± 0.05 , but a significant number of them have confidence bounds between ± 0.07 and ± 0.08 . The uncertain of the measures are related with the number of waveforms utilised and the multiples are seen less consistently among the waveforms, especially the PpSs + PsPs phase.

302

303 Common Conversion Point (CCP) stacking

304 Next, P-wave receiver functions were migrated and stacked in the depth-domain to produce an NE-SW cross-section under the recording network, with the goal of assessing lateral 305 variations in crustal thickness. We followed the approach of Frassetto et al. (2010), this 306 procedure combines the CCP stacking of Gilbert and Sheehan (2004) with the phase-weighting 307

308 scheme of Schimmel and Paulssen (1997) to enhance coherent P-to-S conversions in the
 309 stacks. The geographical locations of the P-to-S conversions — or piercing points — are
 310 then tabulated for each depth, and used to define a grid of uniformly spaced nodes, piercing
 311 points can be visualized in Figure 6-a. The receiver functions are back-projected along ray-
 312 paths containing P-to-S conversions, which effectively migrates the receiver functions into
 313 the depth domain. Back-projection is achieved after ray-tracing through the 1D velocity
 314 model displayed in Figure 6-b. This 1D velocity model was built by averaging the S-wave
 315 velocity models retrieved from Joint Inversion, see next section for more details.

316 The migrated, CCP-stacked cross-section for the for the Parnaíba basin is displayed in
 317 Figure 6. The major discontinuity detected in the cross-section is at 38–44 km depth, Moho
 318 discontinuity. This discontinuity presents a gently slope with a higher values in the center
 319 of the basin, as seen in Figure 6-c. The migrated image generated presents a undifferenti-
 320 ated crustal basement beneath the Parnaíba Basin. The cross-section displays negative
 321 amplitudes covering the crust. These amplitudes are multiples related with the shallow
 322 sedimentary layer, generated due to negative contrast of velocity at the base of this inter-
 323 face. Published results of crustal structure for the Parnaíba Basin based in other geophysical
 324 methods, (de Castro et al., 2014; Daly et al., 2014), identify a deeper crust–mantle boundary,
 325 however, our results presents a Moho deeper than these authors, as well our H- κ stacking
 326 results. Another interesting relation can be observed within the Parnaíba Basin, the Figure
 327 6-c reveals that the eastern side, regions of low topography, is characterized by a thin crust
 328 (38 km), while regions of elevated topography, current depocenter, tend to display a crust
 329 of 41 km or thicker. This behavior is controversial, because is intuitive that the current de-
 330 pocenter needs to be the lowest part of the basin. Additionally, Almeida et al. (2015) report
 331 the same behavior within the Borborema Province. Overall, when we compute the uncer-
 332 tainties in the location of the discontinuities by bootstrapping the receiver function dataset,
 333 Moho presents a almost flat relief, \approx 40 km, as shown with the black segments in Figure 6-c.
 334

335 **Joint inversion with surface-wave dispersion**

336 Finally, S-velocity models beneath individual PBAP stations were developed through
 337 by inverting receiver function waveforms jointly with surface-wave dispersion velocities. We
 338 followed the approach of Julià et al. (2000, 2003), in which state that both receiver functions
 339 and dispersion curves are sensitive to the shear wave velocity of the lithosphere and use this
 340 dataset to generated a S-wave velocity model of the subsurface shear velocity structure.
 341 The procedure includes an influence factor that weights the contribution of each dataset
 342 to the misfit function driving the inversion, this parameter was set of 0.5 to provided a
 343 equal contribuition to each dataset. The starting model adopted for the inversion follow the
 344 assumptions of Julia et al. (2008), a medium perfectly elastic and isotropic with a 40-km
 345 thick crust and a linear S-velocity increase from 3.4 to 4.0 km/s overlying a flattened PREM
 346 model. Smoothness constraints in the velocity profiles are usefull to attenuate instabilities
 347 that drive the iterative process away from convergence.

348 Dispersion velocities were borrowed from the continental-scale, surface-wave tomography
 349 study of Feng et al. (2007). In that study has been collected a large data set for the stable
 350 part of the South American continent and applied a simultaneously inverting regional S and
 351 Rayleigh waveforms and fundamental mode Rayleigh wave group velocities to determine a

352 3-D upper mantle S-wave velocity and Moho depth model for South America. The joint
 353 inversion firstly determine the group velocity maps at different periods and the 1-D average
 354 S velocity structure and Moho depth along each path. Hereafter, it computes the 3-D S
 355 velocity model and Moho depth by combining the regionalized dispersion curves and the 1-D
 356 path-averaged structures, calculated previously. Feng et al. (2007) presented that the Moho
 357 depth ranges from 30 to 70 km beneath the South America continent and high velocities
 358 beneath the Amazon and part of the Paraná and Parnaíba basins with 150 km depth.

359 The performance of the joint inversion procedure is illustrated in Figure 4, through its
 360 application to receiver functions developed for STSN and BUCO stations. The start and
 361 final joint inversion models for both station with the fits between the observed and predicted
 362 receiver function waveforms and Rayleigh-wave dispersion curves are presented in Figure 4.
 363 The starting model was built of thin layers of constant thickness, 0.25 to 1.5 km down to 5
 364 km depth, 2.5 km down to 50 km depth, 5.0 km down to 100 km depth, and 10 km down to
 365 400 km depth, as shown in the gray line in Figure 5-a and d. The starting model allowed a
 366 full detail recovery in both shallow and deeper crust structures and its velocity distribution
 367 prevents instabilities during the inversion process. Ultimately, 9 iterations sufficed for the
 368 inversion process to converge to a final S-wave velocity model. Analysing the fit between
 369 observations and predictions presented we found a good agreement, as shown in Figure 4-
 370 b,c,e and f. Low velocity layers, $> 3.2 \text{ km/s}$, in the top of the final models are observed in
 371 both station, followed by a flattened increasing of the S-wave velocity, $< 4.3 \text{ km/s}$, until \approx
 372 40 km of depth (Figure 4-a,d).

373 The S-velocity models developed for the PBAP stations using the joint inversion ap-
 374 proach are displayed in Figure 5. For comparison, we overlapped the S-velocity inverted
 375 models and the H- κ stacking results of Table 2, adopting Vp of 6.4 km/s . The crustal thick-
 376 nesses from the inverted models, as expected, are in excellent agreement with the thicknesses
 377 inferred from our H- κ stacking analysis and the migrated image, as seen in Figure 6-c. S-wave
 378 velocity colors, sedimentary layer ($> 3.2 \text{ km/s}$), crust (between 3.2 to 4.3 km/s) and mantle
 379 ($< 4.3 \text{ km/s}$) are based in a average S-velocity model calculated using the global crust model
 380 of Mooney et al. (1998). For each station we calculated the S-wave velocity profile, after
 381 that, we averaged these models to provide a S-wave velocity reference. S-wave velocity mod-
 382 els shows the same behavior of the crust structure observed in Figure 6-c, a nondifferentiable
 383 crust, with a smoothed increasing of the S-wave velocity (gray color). The inversion been able
 384 to recover the sedimentary structure (white color) correctly, mainly the average thickness of
 385 the basin $\approx 3 \text{ km}$ (dashed line), according to Vaz et al. (2007). Under the stations PRDT and
 386 STSR was observed a low velocity layer composed of velocities between 3.3 to 3.5 km/s at
 387 the interval of 10 to 17 km depth. In addition, these stations are localized above the location
 388 of the Parnaíba block midcrustal reflectors marked by Daly et al. (2014) at $\approx 15 \text{ km}$ depth.

389

390

391 Tectonic implications

392 The crustal thickness and velocity structure across the Parnaíba basin from its west to
 393 the east border is presented based on H- κ stacking, CCP migration and joint inversion of
 394 receiver function and Rayleigh wave group velocity. Analysing the results we point important
 395 findings: (1) a relative flatness of the crust-mantle boundary at depths of 40-43 km under

396 the central portion of the Parnaíba basin is observed for the first time; (2) a homogeneous
 397 crust with no evidence of large inner crustal discontinuities; (3) the velocity models for the
 398 basin's underlying crust displayed little lateral variation in crustal velocity along the profile,
 399 consistent with the presence of a uniform, central cratonic block; (4) a thinning crust towards
 400 the eastern flank, bounding with the Borborema Province, is observed in S-wave velocity
 401 models and in migrated cross-section; (5) the western part of the basin presents a thickest
 402 crust comparing with the results of Daly et al. (2014), ≈ 40 km. Based on the cited results,
 403 we verified the crustal thickening along the central part of the basin. The crustal stretching
 404 no longer affect subsidence of the basin, probably it acted in the early stages of the basin
 405 formation.

406 Our results on crustal thickness for the Parnaíba basin are at odds with models of basin
 407 evolution that invoke an initial mechanical stretching of the basin's lithosphere. According
 408 the provided images and S-wave velocity models of the crustal structure the rifting episode
 409 during the evolution of the basin was not strong enough to affect the crustal thickness on a
 410 regional scale. Consequently, the subsidence of the basin is related majoritarily with thermal
 411 process, as well as happened the thermal subsidence of the Congo basin in the Paleozoic
 412 period (Daly et al., 1992).

413 This range of V_p/V_s values is compatible with a bulk felsic composition (Christensen,
 414 1996), but the large confidence bounds actually allow for a broader range of crustal compo-
 415 sitions. A important feature that we can observe is that the Table 2 indicates an increment
 416 of V_p/V_s ratio with increasing crustal thickness, probably associated with the growth the
 417 mafic lower crust (Christensen, 1996). The same behavior is observed by Chevrot and van der
 418 Hilst (2000) in the Australian crust. Similarly, Christensen (1996) and Julia et al. (2008)
 419 suggest that high values can be related with a mafic crust or a concentration of basaltic
 420 rocks, correlating with gross thickness of diabase intrusions in the center of the basin. Daly
 421 et al. (2014) recognise the shallower anastomosing discontinuity, called midcrustal reflector,
 422 in the same place that the stations PRDT and STSR presents a relative low velocity layer
 423 at ≈ 15 km. This velocity contrast can be associated with a concentration of basaltic rocks
 424 in basement structures. According to Durrheim and Mooney (1991, 1994) a layer with a
 425 seismic velocity greater than 4.0 km/s (probably representing predominantly mafic rocks)
 426 composes only 5%-10% of the Archean crust, but is typically 20%-30% of the Proterozoic
 427 crust. As seen in Figure 5, just a thin layer in our profile can reach velocities higher than
 428 4.0 km/s suggesting a block beneath the Parnaíba basin with Archean age.

429 The lack of a large mafic lower crust in the central Parnaíba block is also consistent with
 430 a purely thermal origin for the subsidence of the Parnaíba basin. According to ours S-wave
 431 velocity models, the mafic layer (velocities higher than 4.0 km/s) in the lower crust reaches
 432 only to 2 km height. Thus, a subsidence model that postulate a large load in the lower crust
 433 cannot describe genuinely the mechanism of formation of the Parnaíba basin, differently of
 434 the Paraná basin subsidence mechanism (Julia et al., 2008). The proposal is that the loads
 435 who drives the subsidence should be in lithosphere, instead of the crust.

436 Nonetheless, thermal subsidence might not be the only process capable of explaining
 437 subsidence of this large cratonic basin of South America. As some cratonic basins of Africa,
 438 the mantle convection has a important role in the formation of cratonic basins and deserves
 439 further attention. In particular, models involving uplifts, which may be related to convective
 440 upwellings, and cold-spots associated with convective downwellings, may be helpful in
 441 explaining the origin of regional subsidence in space and time (Hartley and Allen, 1994). But

442 to investigate the lithosphere structure is necessary to add more data from regional studies.

443

444

445 Conclusions

446 The Parnaíba Basin is an example of an intracratonic basin located over a thick crust
 447 and with a depositional history composed by several periods of uplift and erosion in its
 448 long geological history. Summarizing, we have obtained 9 point estimates of crustal thick-
 449 ness and bulk Vp/Vs ratio across the Parnaíba basin of NE Brazil. S-velocity models and
 450 cross-section of a migrated P-wave receiver functions in the Parnaíba Basin have demon-
 451 strated the existence of the major seismic discontinuity characterizing the crustal archi-
 452 tecture of the basin. The deeper discontinuity displays values ranging between 38 and
 453 44 km, and has been identified with the crust–mantle boundary. We provided a seismic
 454 evidence of the crustal architecture of the thick block beneath of the Parnaíba basin, as
 455 proposed Brito Neves et al. (1984); Fuck et al. (2008); Cordani et al. (2009); Daly et al.
 456 (2014). Although our result, mainly the S-wave velocity models, suggest the presence
 457 of a Archean cratonic nucleus under the basin, conflicting with previous geological stud-
 458 ies. Crustal stretching cannot explain variations in the subsidence and exhumation his-
 459 tories of the basin, because the crust was thickening along the time generating a thick
 460 crust. The thermal mechanism is more acceptable due to the lack of a massive lower
 461 crust, not to mention the gross thickness of diabase intrusions in the center of the basin.

462

463

464 Acknowledgements

465 Acquisition and analysis of the dataset presented in this study was funded through a
 466 grant awarded by BP Energy do Brasil (grant number XXXXXXXXX). D.L.O.C. addition-
 467 ally thanks BP Energy do Brasil for awarding a scholarship to complete his PhD degree at the
 468 Universidade Federal do Rio Grande do Norte. JJ also thanks BP Energy do Brasil for award-
 469 ing a research fellowship to conduct this research.

470

471

472 References

- 473 Almeida, F. F. M., Y. Hasui, B. B. Brito Neves, and R. A. Fuck, 1981, Brazilian structural
 474 provinces: An introduction: *Earth Science Reviews*, **17**, 1–29.
- 475 Almeida, Y. B., J. Julià, and A. Frassetto, 2015, Crustal architecture of the borborema
 476 province, NE brazil, from receiver function CCP stacks: Implications for mesozoic stretch-
 477 ing and cenozoic uplift: *Tectonophysics*, **649**, 68–80.
- 478 Ammon, C. J., 1991, The isolation of receiver effects from teleseismic p waveforms: *Bulletin*
 479 of the Seismological Society of America
- 480 Ammon, C. J., G. E. Randall, and G. Zandt, 1990, On the nonuniqueness of receiver function
 481 inversions: *Journal of Geophysical Research*, **95**, no. B10, 15303–15318.

- 482 Assumpção, M., M. Bianchi, J. Julià, F. L. Dias, G. Sand França, R. Nascimento, S. Drouet,
 483 C. G. Pavão, D. F. Albuquerque, and A. E. V. Lopes, 2013a, Crustal thickness map of
 484 brazil: Data compilation and main features: *Journal of South American Earth Sciences*,
 485 **43**, 74–85.
- 486 Assumpção, M., M. Feng, A. Tassara, and J. Julià, 2013b, Models of crustal thickness for
 487 south america from seismic refraction, receiver functions and surface wave tomography:
 488 *Tectonophysics*, **609**, 82–96.
- 489 Brito Neves, B., R. Fuck, U. Cordani, and F. Thomaz, 1984, Influence of basement structures
 490 on the evolution of the major sedimentary basins of brazil: A case of tectonic heritage:
 491 *Journal of Geodynamics*, **1**, 495–510.
- 492 Brito Neves, B. B., and R. A. Fuck, 2013, Neoproterozoic evolution of the basement of the
 493 south-american platform: *Journal of South American Earth Sciences*, **47**, 72–89.
- 494 Brito Neves, B. B. d. B., and R. A. Fuck, 2014, The basement of the south american platform:
 495 Half laurentian (n-NW)+half gondwanan (e-SE) domains: *Precambrian Research*, **244**,
 496 75–86.
- 497 Cassidy, J. F., 1992, Numerical experiments in broadband receiver function analysis: *Bulletin of the Seismological Society of America*, **82**, 1453–1474.
- 498 Chevrot, S., and R. D. van der Hilst, 2000, The poisson ratio of the australian crust: geological and geophysical implications: *Earth and Planetary Science Letters*, **183**, 121 – 132.
- 502 Christensen, N. I., 1996, Poisson's ratio and crustal seismology: *Journal of Geophysical Research*, **101**, 3139–3156.
- 504 Cloetingh, S., and E. Burov, 2011, Lithospheric folding and sedimentary basin evolution: a
 505 review and analysis of formation mechanisms: *Basin Research*, **23**, 257–290.
- 506 Cordani, U., B. Brito Neves, and T. F. A., 2009, Estudo preliminar de integração do pré-
 507 cambriano com os eventos tectônicos das bacias sedimentares brasileiras(atualização): Bo-
 508 letim de Geociências da Petrobras, **17**, 205–219.
- 509 Cordani, U. G., M. M. Pimentel, G. d. Araujo, C. Eduardo, and R. A. Fuck, 2013, The
 510 significance of the transbrasiliiano-kandi tectonic corridor for the amalgamation of west
 511 gondwana: *Brazilian Journal of Geology*, **43**, 583.
- 512 Daly, M. C., V. Andrade, C. A. Barousse, R. Costa, K. McDowell, N. Piggott, and A. J.
 513 Poole, 2014, Brasiliiano crustal structure and the tectonic setting of the parnaíba basin of
 514 NE brazil: Results of a deep seismic reflection profile: *Tectonics*, **33**, 2014TC003632.
- 515 Daly, M. C., S. R. Lawrence, K. Diemu-Tshiband, and B. Matouana, 1992, Tectonic evolution
 516 of the cuvette centrale, zaire: *Journal of the Geological Society*, **149**, 539–546.
- 517 de Castro, D. L., F. H. Bezerra, R. A. Fuck, and R. M. Vidotti, 2016, Geophysical evidence
 518 of pre-sag rifting and post-rifting fault reactivation in the parnaíba basin, brazil: *Solid
 519 Earth*, **7**, 529–548.
- 520 de Castro, D. L., R. A. Fuck, J. D. Phillips, R. M. Vidotti, F. H. R. Bezerra, and E. L.
 521 Dantas, 2014, Crustal structure beneath the paleozoic parnaíba basin revealed by airborne
 522 gravity and magnetic data, brazil: *Tectonophysics*, **614**, 128–145.
- 523 Durrheim, R. J., and W. D. Mooney, 1991, Archean and proterozoic crustal evolution:
 524 Evidence from crustal seismology: *Geology*, **19**, 606–609.
- 525 ———, 1994, Evolution of the precambrian lithosphere: *Seismological and geochemical con-
 526 straints: Journal of Geophysical Research*, **99**, no. B8, 15359–15374.
- 527 Efron, B., and R. Tibshirani, 1991, Statistical data analysis in the computer age: *Science*,
 528 **253**, 390–395.
- 529 Fairhead, J., and S. Maus, 2003, CHAMP satellite and terrestrial magnetic data help define

- 530 the tectonic model for south america and resolve the lingering problem of the pre-break-up
 531 fit of the south atlantic ocean: *The Leading Edge*, **22**, 779–783.
- 532 Feng, M., M. Assumpção, and S. Van der Lee, 2004, Group-velocity tomography and litho-
 533 spheric s-velocity structure of the south american continent: *Physics of the Earth and*
 534 *Planetary Interiors*, **147**, 315–331.
- 535 Feng, M., S. van der Lee, and M. Assumpção, 2007, Upper mantle structure of south america
 536 from joint inversion of waveforms and fundamental mode group velocities of rayleigh
 537 waves: *Journal of Geophysical Research*, **112**, no. B4, B04312.
- 538 Frassetto, A., G. Zandt, H. Gilbert, T. J. Owens, and C. H. Jones, 2010, Improved imaging
 539 with phase-weighted common conversion point stacks of receiver functions: *Geophysical*
 540 *Journal International*, **182**, 368–374.
- 541 Fuck, R. A., B. B. Brito Neves, and C. Schobbenhaus, 2008, Rodinia descendants in south
 542 america: *Precambrian Research*, **160**, 108–126.
- 543 Gilbert, H. J., and A. F. Sheehan, 2004, Images of crustal variations in the intermountain
 544 west: *Journal of Geophysical Research*, **109**, no. B3, B03306.
- 545 Góes, A., and F. Feijó, 1994, Bacia do parnaíba: *Boletim de Geociências da Petrobras*, **8**,
 546 57–67.
- 547 Hartley, R. W., and P. A. Allen, 1994, Interior cratonic basins of africa: relation to conti-
 548 nental break-up and role of mantle convection: *Basin Research*, **6**, 95–113.
- 549 Julia, J., M. Assumpcao, and M. P. Rocha, 2008, Deep crustal structure of the parana basin
 550 from receiver functions and rayleigh-wave dispersion: Evidence for a fragmented cratonic
 551 root: *Journal of Geophysical Research*, **113**, no. B8.
- 552 Julià, J., C. J. Ammon, and R. B. Herrmann, 2003, Lithospheric structure of the arabian
 553 shield from the joint inversion of receiver functions and surface-wave group velocities:
 554 *Tectonophysics*, **371**, 1–21.
- 555 Julià, J., C. J. Ammon, R. B. Herrmann, and A. M. Correig, 2000, Joint inversion of receiver
 556 function and surface wave dispersion observations: *Geophysical Journal International*,
 557 **143**, 99–112.
- 558 Kaminski, E., and C. Jaupart, 2000, Lithosphere structure beneath the phanerozoic intracra-
 559 tonic basins of north america: *Earth and Planetary Science Letters*, **178**, 139–149.
- 560 Klein, E. L., C. A. V. Moura, R. S. Krymsky, and W. L. Griffin, 2005, The gurupi belt,
 561 northern brazil: lithostratigraphy, geochronology, and geodynamic evolution: *Precam-
 562 brian Research*, **141**, 83–105.
- 563 Langston, C. A., 1979, Structure under mount rainier, washington, inferred from teleseismic
 564 body waves: *Journal of Geophysical Research*, **84**, no. B9, 4749–4762.
- 565 Ligorría, J. P., and C. J. Ammon, 1999, Iterative deconvolution and receiver-function esti-
 566 mation: *Bulletin of the Seismological Society of America*, **89**, 1395–1400.
- 567 Lloyd, S., S. van der Lee, G. S. França, M. Assumpção, and M. Feng, 2010, Moho map of
 568 south america from receiver functions and surface waves: *Journal of Geophysical Research:*
 569 *Solid Earth*, **115**, n/a–n/a.
- 570 Mooney, W. D., G. Laske, and T. G. Masters, 1998, CRUST 5.1: A global crustal model at
 571 $5^\circ \times 5^\circ$: *Journal of Geophysical Research*, **103**, no. B1, 727–747.
- 572 Owens, T. J., G. Zandt, and S. R. Taylor, 1984, Seismic evidence for an ancient rift be-
 573 neath the cumberland plateau, tennessee: A detailed analysis of broadband teleseismic p
 574 waveforms: *Journal of Geophysical Research*, **89**, no. B9, 7783–7795.
- 575 Schimmel, M., and H. Paulssen, 1997, Noise reduction and detection of weak, coherent
 576 signals through phase-weighted stacks: *Geophysical Journal International*, **130**, 497–505.
- 577 Uieda, L., and V. C. F. Barbosa, 2017, Fast nonlinear gravity inversion in spherical coordi-

- 578 nates with application to the south american moho: Geophysical Journal International,
579 **208**, 162–176.
- 580 van der Meijde, M., J. Julià, and M. Assumpção, 2013, Gravity derived moho for south
581 america: Tectonophysics, **609**, 456–467.
- 582 Vaz, P., N. Rezende, F. J. W., and W. Travassos, 2007, Bacia do parnaíba: Boletim de
583 Geociências da Petrobras, **15**, 253–263.
- 584 Zhu, L., and H. Kanamori, 2000, Moho depth variation in southern california from teleseismic
585 receiver functions: Journal of Geophysical Research, **105**, no. B2, 2969–2980.

⁵⁸⁶ **Tables**

Table 1: *Station coordinates and recording time window from Parnaíba basin.*

Station	Latitude	Longitude	Recording time
BPPF	-6.2271	-47.2518	2016.188 – 2016.345
BUCO	-5.1586	-43.2010	2016.118 – 2016.344
GENI	-5.4612	-45.5344	2016.105 – 2016.346
GRJU	-5.8308	-46.0882	2016.104 – 2016.345
PRDT	-5.3241	-44.3974	2016.106 – 2016.344
STSN	-6.0787	-46.5986	2016.105 – 2016.345
STSР	-5.2889	-43.8063	2016.119 – 2016.344
TRSN	-5.1056	-42.6344	2016.118 – 2016.344
BDCO	-5.4517	-45.0203	2015.222 – 2016.293

Table 2: H - κ stacking parameters and results to different values of Vp from *Parnaíba basin*.

Station	n	w1,w2,w3	H (km) $\pm \epsilon$							$Vp/Vs \pm \epsilon$
			Vp 6.3	Vp 6.4	Vp 6.5	Vp 6.6	Vp 6.7	Vp 6.3	Vp 6.4	
BPPF	5	0.5,0.5,0.0	41.4 \pm 2.2	42.2 \pm 3.0	42.7 \pm 3.2	43.5 \pm 2.3	44.5 \pm 2.2	1.75 \pm 0.05	1.74 \pm 0.05	1.74 \pm 0.04
BUCO	11	0.4,0.3,0.3	38.0 \pm 0.8	38.7 \pm 0.7	39.5 \pm 0.8	40.4 \pm 0.9	41.0 \pm 1.4	1.73 \pm 0.03	1.72 \pm 0.03	1.71 \pm 0.03
GENI	7	0.5,0.5,0.0	43.7 \pm 1.4	44.7 \pm 2.5	45.5 \pm 1.9	46.4 \pm 1.9	47.2 \pm 1.5	1.76 \pm 0.05	1.75 \pm 0.05	1.75 \pm 0.06
GRJU	11	0.4,0.3,0.3	40.9 \pm 1.8	41.7 \pm 1.9	42.5 \pm 2.2	43.2 \pm 1.7	44.0 \pm 1.3	1.83 \pm 0.05	1.82 \pm 0.05	1.81 \pm 0.05
PRDT	11	0.4,0.3,0.3	38.7 \pm 3.3	39.5 \pm 3.5	40.2 \pm 3.6	41.0 \pm 3.5	41.9 \pm 3.6	1.81 \pm 0.09	1.80 \pm 0.09	1.80 \pm 0.09
STS N	12	0.4,0.3,0.3	40.4 \pm 1.8	41.2 \pm 2.2	42.0 \pm 2.5	42.7 \pm 2.6	44.0 \pm 1.5	1.75 \pm 0.04	1.75 \pm 0.05	1.74 \pm 0.05
STSR	8	0.4,0.3,0.3	38.5 \pm 0.2	39.4 \pm 0.2	40.2 \pm 0.2	40.9 \pm 0.3	41.7 \pm 0.3	1.69 \pm 0.01	1.68 \pm 0.01	1.68 \pm 0.01
TRSN	12	0.4,0.3,0.3	38.0 \pm 2.8	38.9 \pm 2.8	39.7 \pm 3.0	40.4 \pm 2.8	41.2 \pm 3.3	1.75 \pm 0.07	1.74 \pm 0.07	1.73 \pm 0.06
BDCO	3	0.4,0.3,0.3	40.0 \pm 3.2	40.7 \pm 3.4	41.5 \pm 3.3	42.5 \pm 3.3	43.2 \pm 3.3	1.70 \pm 0.07	1.69 \pm 0.08	1.68 \pm 0.07

* The table includes the number of waveforms (n), P-wave velocity assumed (Vp), weights for the Ps (w1), PpPs (w2), and PpPs + PsPs (w3) phases, respectively.

587 Figures Captions

588 **Fig. 1.** Geological Map with the location of PBAP project stations. AM, Amazonian
 589 Craton; BB, Borborema Province; SF, São Francisco Craton; SL, São Luís Craton; TO,
 590 Tocantins Province.

591 **Fig. 2.** Stacked receiver functions in the Parnaíba basin calculated with Gaussian filter
 592 width $a = 2.5$. Right and left panels show radial and transversal receiver functions, respec-
 593 tively, for each station. The number of waveforms stacked for each station are presented
 594 in round brackets. The maximum and minimum amplitude values of the receiver functions
 595 utilised are plotted in shaded gray.

596 **Fig. 3.** Moisaic showing $H-\kappa$ stacking results for STSR (top) and GRJU (bottom)
 597 stations. a-c) display the receiver function stacked with the Ps, PpPs, and PpSs+PsPs
 598 phases times superimposed to the receiver functions and a figure showing the $H-\kappa$ stacking
 599 screen adopting a V_p of 6.3 km/s . b-d) display the receiver function, radial (black lines)
 600 and tranverse (red lines), sorted by backazimuth and at the right corner a map with the
 601 location of the earthquakes utilised (stars).

602 **Fig. 4.** Joint inversion panels for STSN and BUCO stations. a-d) display the initial
 603 and final S-velocity models; b-e) fits between the receiver functions observed and predicted;
 604 e-f) fits between the group velocities observed and predicted.

605 **Fig. 5.** Joint inversion models for each station sorted according the station location in
 606 Figure 1. Colors represent S-wave velocities: The sedimentary layer, $> 3.2 \text{ km/s}$ (white);
 607 crust, between 3.2 to 4.3 km/s (gray); and mantle, $< 4.3 \text{ km/s}$ (dark gray). These values
 608 are based in models calculated from Mooney et al. (1998). Dashed line represents the 3 km
 609 depth and the black segments are the $H-\kappa$ stacking results with error estimates, Adopting a
 610 V_p of 6.4 km/s .

611 **Fig. 6.** Mosaic with the piercing points map, S-wave velocity model and the migrated
 612 cross-section. a) map with the seismic stations (black triangles), piercing points of the
 613 CCP migration (open circles) and CCP profile (black line). b) average S-wave velocity
 614 model for the PBAP stations. c) color-coded receiver function stacked amplitudes. Red
 615 colors indicate positive amplitudes (i.e., positive velocity contrast), while blue colors indicate
 616 negative amplitudes (i.e., negative velocity contrast). The black segments mark the location
 617 of the Moho Ps conversion at the crust–mantle boundary from bootstrapping.

618 **Figures**

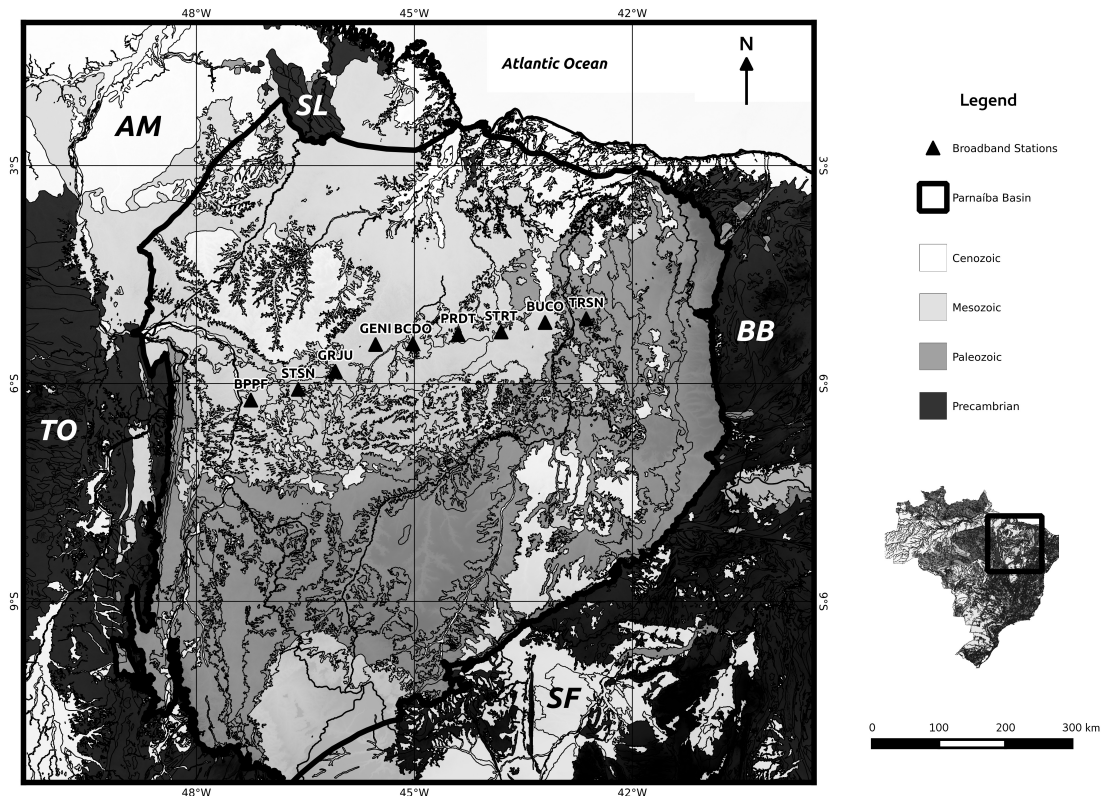


Figure 1: Geological Map with the location of PBAP project stations. AM, Amazonian Craton; BB, Borborema Province; SF, São Francisco Craton; SL, São Luís Craton; TO, Tocantins Province.

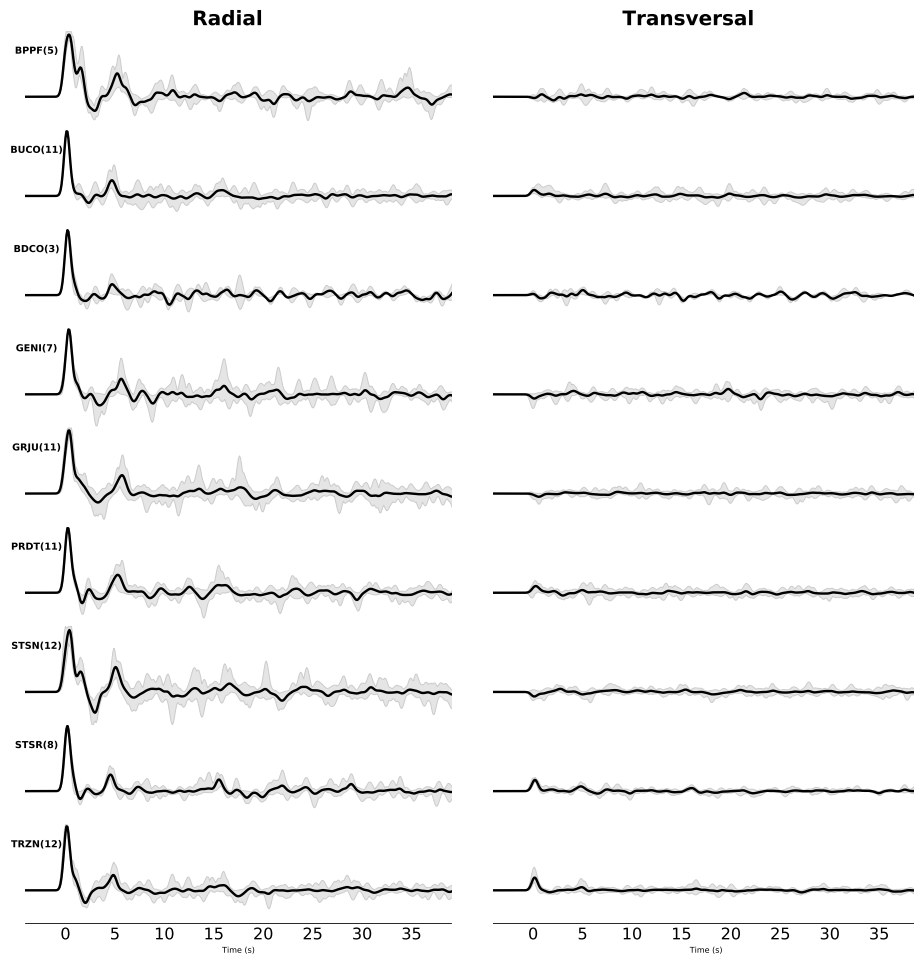


Figure 2: Stacked receiver functions in the Parnaíba basin calculated with Gaussian filter width $a = 2.5$. Right and left panels show radial and transversal receiver functions, respectively, for each station. The number of waveforms stacked for each station are presented in round brackets. The maximum and minimum amplitude values of the receiver functions utilised are plotted in shaded gray.

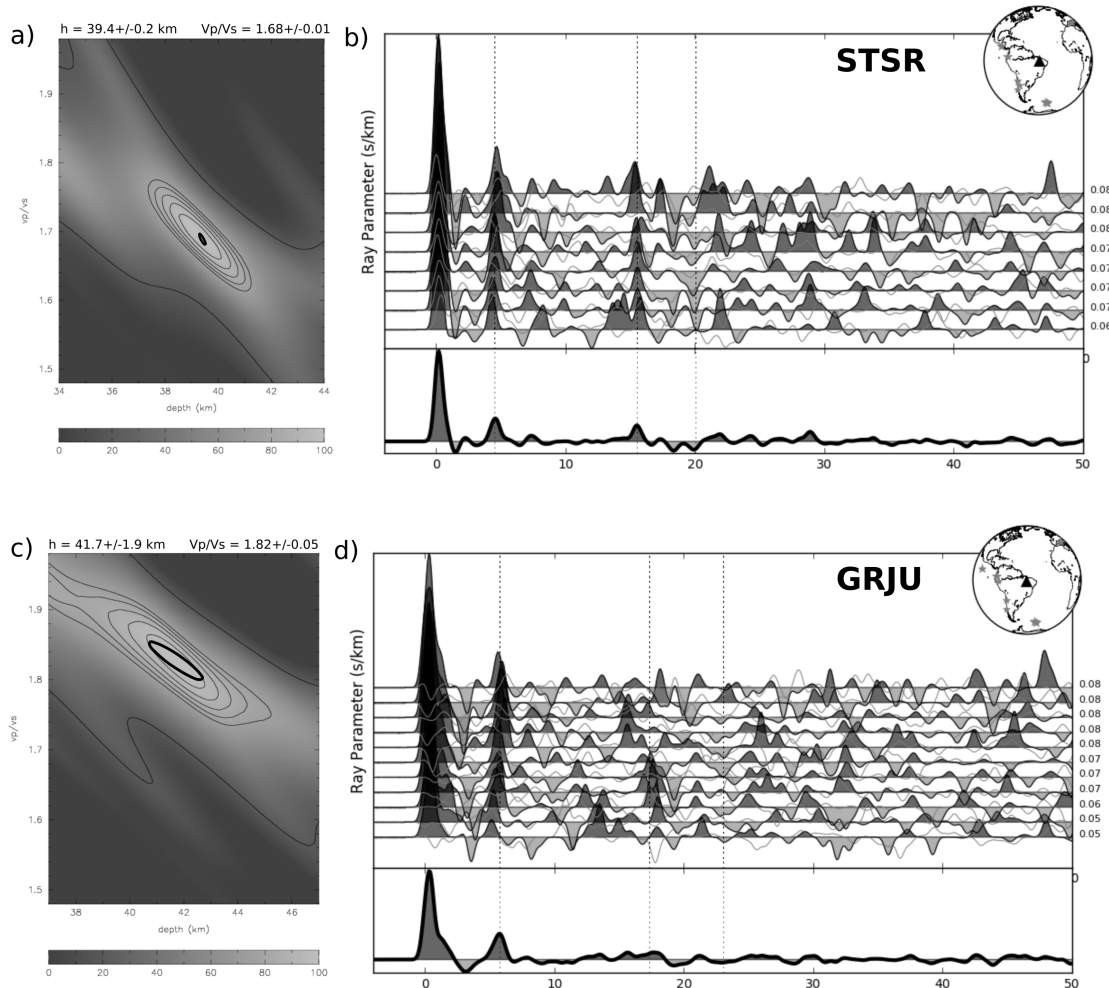


Figure 3: Moisaisc showing $H\text{-}\kappa$ stacking results for STSR (top) and GRJU (bottom) stations. a-c) display the receiver function stacked with the P_s , P_pP_s , and $P_pS_s + P_sP_s$ phases times superimposed to the receiver functions and a figure showing the $H\text{-}\kappa$ stacking screen adopting a V_p of 6.3 km/s. b-d) display the receiver function, radial (black lines) and tranverse (red lines), sorted by backazimuth and at the right corner a map with the location of the earthquakes utilised (stars).

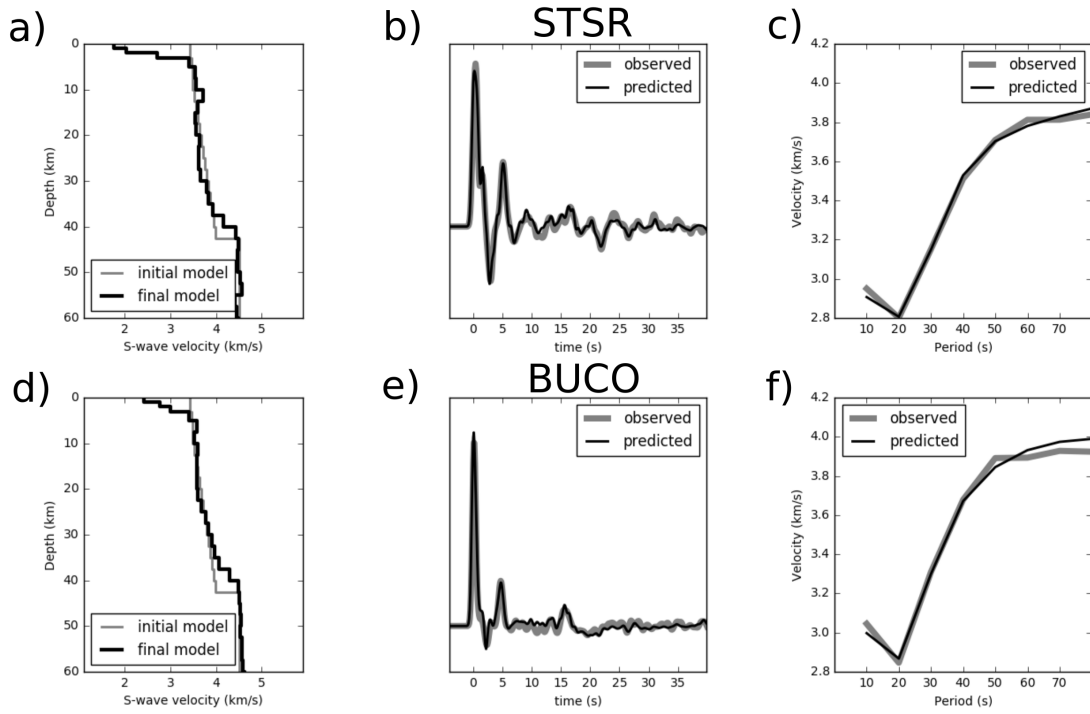


Figure 4: Joint inversion panels for STSN and BUCO stations. a-d) display the initial and final S-velocity models; b-e) fits between the receiver functions observed and predicted; e-f) fits between the group velocities observed and predicted.

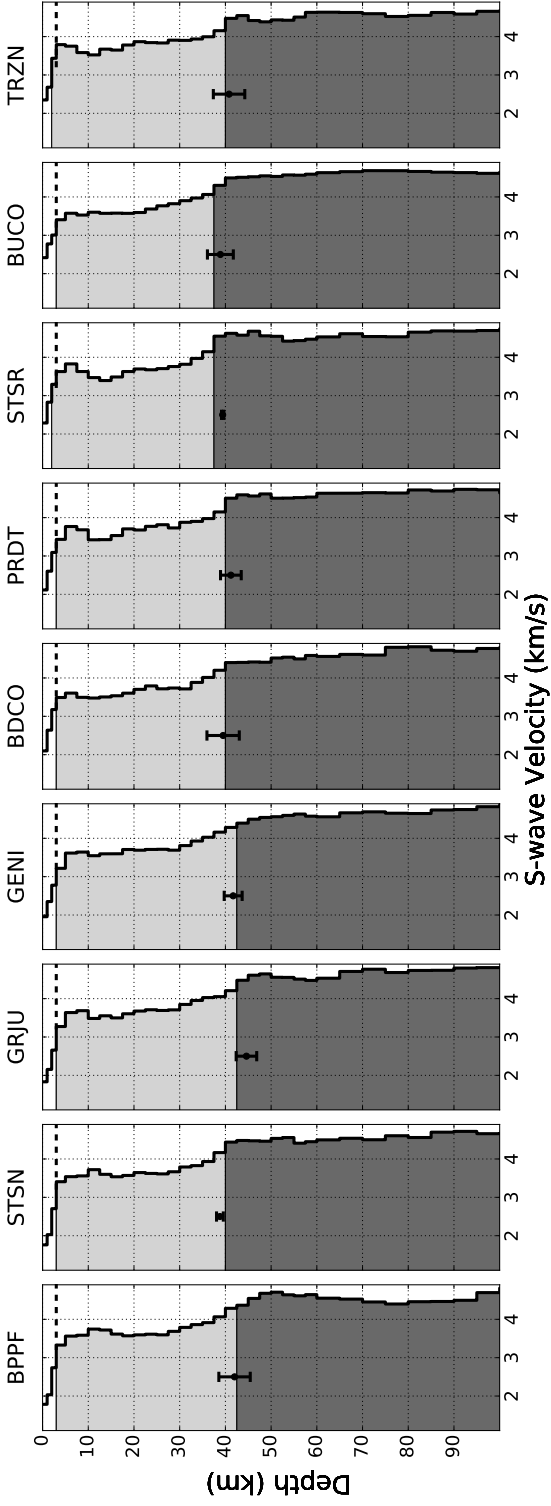


Figure 5: Joint inversion models for each station sorted according the station location in Figure 1. Colors represent S-wave velocities: The sedimentary layer, $> 3.2 \text{ km/s}$ (white); crust, between 3.2 to 4.3 km/s (gray); and mantle, $< 4.3 \text{ km/s}$ (dark gray). These values are based in models calculated from Mooney et al. (1998). Dashed line represents the 3 km depth and the black segments are the H- κ stacking results with error estimates. Adopting a V_p of 6.4 km/s.

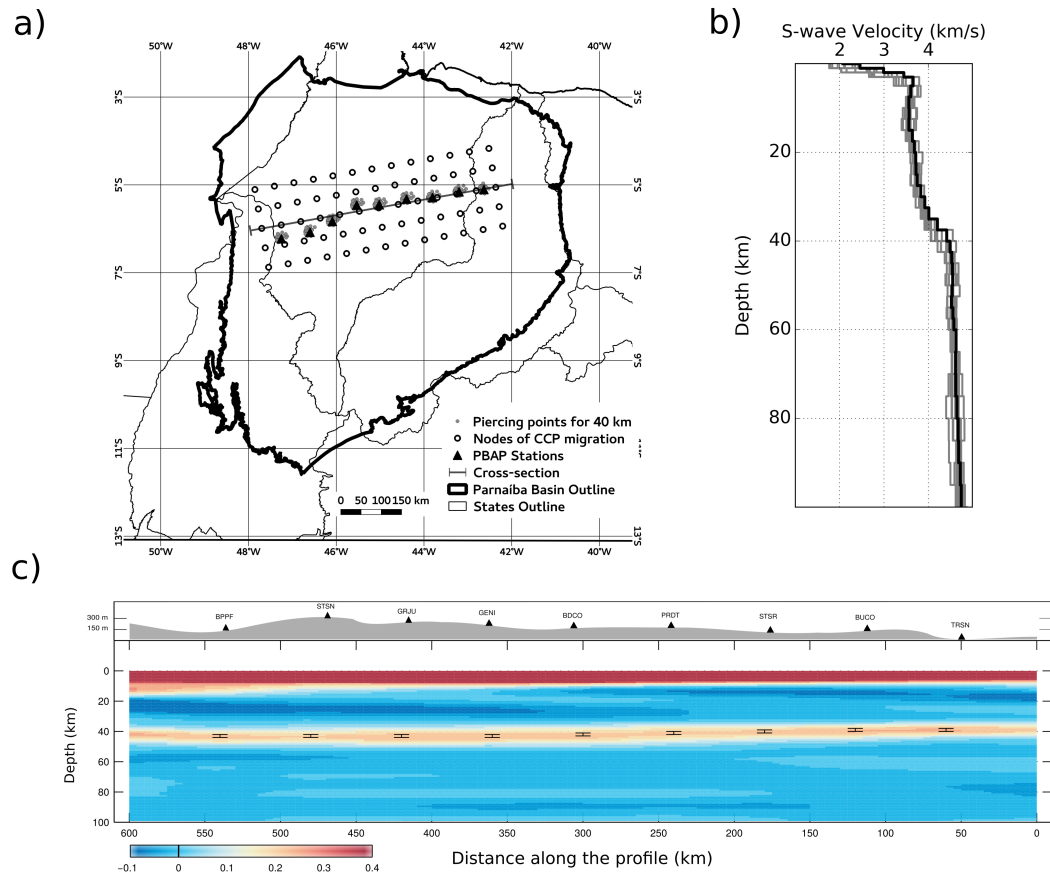


Figure 6: Mosaic with the piercing points map, S-wave velocity model and the migrated cross-section. a) map with the the seismic stations (black triangles), piercing points of the CCP migration (open circles) and CCP profile (black line). b) average S-wave velocity model for the PBAP stations. c) color-coded receiver function stacked amplitudes. Red colors indicate positive amplitudes (i.e., positive velocity contrast), while blue colors indicate negative amplitudes (i.e., negative velocity contrast). The black segments mark the location of the Moho Ps conversion at the crust–mantle boundary from bootstrapping.